Glacial Isostatic Adjustment reduces past and future Arctic subsea permafrost

R. Creel[1], F. Miesner[2], S. Wilkenskjeld[3], J. Austermann[1], and P. P. Overduin[2]

[1]Lamont-Doherty Earth Observatory, Columbia University, New York, USA
[2]Alfred Wegener Institute Helmholtz-Centre for Polar and Marine Research, Potsdam, Germany
[3]Max Planck Institute for Meteorology, Hamburg, Germany

NB: This is a non-peer reviewed EarthArXiv preprint submitted to Nature Communications

Corresponding author: Roger Creel, rcc2167@columbia.edu

Abstract

Sea-level rise submerges terrestrial permafrost in the Arctic, turning it into subsea permafrost. Subsea permafrost underlies ∼1.8 million km^2 of Arctic continental shelf, with thicknesses in places exceeding 700 m. Sea-level variations over glacial-interglacial cycles control subsea permafrost distribution and thickness, yet no permafrost model has accounted for glacial isostatic adjustment (GIA), which deviates local sea level from the global mean due to changes in ice and ocean loading. We incorporate GIA into a pan-Arctic model of subsea permafrost over the last 400,000 years. Including GIA significantly reduces present-day subsea permafrost thickness, chiefly because of hydro-isostatic effects as well as deformation related to Northern Hemisphere ice sheets. Additionally, we extend the simulation 1000 years into the future for emissions scenarios outlined in the International Panel on Climate Change's sixth assessment report. We find that subsea permafrost is preserved under a low emissions scenario but mostly disappears under a high emissions scenario.

1 Introduction

Sea-level lowstands during past glacial periods exposed the Arctic continental shelf to cold air temperatures that froze the ground, forming up to a kilometer of new permafrost (Schirrmeister et al., 2011). Postglacial sea-level rise inundated much of this cryotic sediment, producing subsea permafrost, which began to thaw as oceanic heat and salt propagated downwards from the seafloor (Romanovskii et al., 2004). Permafrost is defined here as sediment above or below sea level that has temperature at or below 0 °C for at least two years and may or may not contain ice. While present-day subsea permafrost thaws due to geothermal heat from below and ocean warming from above, more is created at an accelerating rate as terrestrial permafrost turns into subsea permafrost through coastal erosion (Jones et al., 2009) and sea-level rise (Proshutinsky et al., 2001, 2004).

The need to track human carbon dioxide emissions (CO_2) has driven assessments of the global carbon budget, including the amount and stability of the carbon reservoir below the ocean floor (Friedlingstein et al., 2020, 2022). Ongoing debate surrounding how much carbon from thawing subsea permafrost will reach the atmosphere (Ruppel & Kessler, 2017; Shakhova et al., 2014; P. Overduin et al., 2016) has precluded subsea permafrost's inclusion in global carbon budgets. Recent work and structured expert assessment, however, suggest that the submarine permafrost domain holds an amount of carbon in organic matter and methane hydrates of similar magnitude to the Earth's total gas reserves (Sayedi et al., 2020; Ruppel & Kessler, 2017; Gilfillan et al., 2019). Rising Arctic water temperatures in the coming century, projected under all emissions scenarios, will hasten subsea permafrost thaw (Wilkenskjeld et al., 2021). Accelerated permafrost thaw rates will increase carbon mobilization rates beneath the seabed. Since this carbon may reach the atmosphere as greenhouse gas, it is important to have an estimate for the amount of carbon currently trapped in and by permafrost, its stability, and the timing of its release.

Such an estimate requires accurate quantification of how much subsea permafrost exists today. Regional maps of present subsea permafrost extent typically rely on a combination of observations and physics-based modeling (D. J. Nicolsky et al., 2012; Brothers et al., 2016). The International Permafrost Association (IPA) permafrost map, an early pan-Arctic effort, applied the heuristic that permafrost would exist anywhere where the shelf was exposed for long enough during sea-level lowstands to establish permafrost, implying unglaciated regions shallower than around 100 m (Brown et al., 1997). More recently, subsea permafrost was mapped in a consistent manner at circum-Arctic spatial scale over the last 450 thousand years (P. P. Overduin et al., 2019) by forcing a heat transfer model with spatially-varying geothermal heat flux, depth-varying ocean bottom water temperature, sediment porosity, global mean sea level (GMSL) from a Red Sea oxygen isotope record (Grant et al., 2014), and ice sheet thicknesses and air temperature from the CLIMBER2 Earth System Model (Ganopolski et al., 2010).

Sea level and ice history are the most important controls on subsea permafrost formation. Together, they determine the fraction of time Arctic sediments are exposed to (relatively) warm temperatures beneath ice sheets or oceans rather than to cold air temperature. In Arctic shelf regions beyond the maximal extents of the Northern Hemispheric ice sheets, inundation time controls the distribution, depth, and density of subsea permafrost (Angelopoulos et al., 2020). Extant subsea permafrost calculations have included GMSL as a forcing term (Romanovskii et al., 2004; P. P. Overduin et al., 2019; D. Nicolsky & Shakhova, 2010). However, local sea level at locations on the Arctic shelf deviates from GMSL (Klemann et al., 2015) due to glacial isostatic adjustment (GIA), which is the gravitational, deformational, and rotational response of the solid Earth to ice and liquid water loading (Farrell & Clark, 1976). In the GIA literature, local sea level is also often referred to as relative sea level (RSL), which is defined as sea level at a given location and time relative to present-day sea level at the same location.

The deviation between local and global mean sea level is particularly pronounced near Banks Island and in the Barents and Kara Seas—where ice sheet loading deformed the solid earth by hundreds of meters over glacial cycles—and along the western Laptev Sea and North Slope, which underwent peripheral bulge uplift and subsidence (Lambeck, 1995; Lakeman & England, 2014). Even in places far from the Northern Hemisphere ice sheets at Last Glacial Maximum (LGM, ∼26.5 to 19 thousand years before present (kyr BP)), such as the East Siberian Sea, changing water loading over glacial cycles can cause RSL to deviate from GMSL by 10+ meters (Klemann et al., 2015). Since these changes in local sea-level history can lengthen or shorten the duration of land inundation or seabed exposure for large portions of the Arctic shelf, we hypothesize that their omission leads to nonuniform biases in estimates of subsea permafrost distribution, thickness, and thaw rate.

Here we test this hypothesis by extending the subsea permafrost model of P. P. Overduin et al. (2019) to include RSL produced by GIA modeling. We isolate the effects of GIA by comparing permafrost extents from a simulation that includes spatially varying RSL to two that do not. We explore whether the inclusion of GIA in numerically modeled subsea permafrost improves correspondence between modeled and measured subsea permafrost extent. We further explore the effect of future warming scenarios on subsea permafrost distribution by extending models that do and do not include GIA to year 3000 under a range of ice melt scenarios related to shared socioeconomic pathways (SSPs, hereafter 'emissions pathways') from the International Panel on Climate Change's 6$^{\text{th}}$ Assessment report (IPCC, Fox-Kemper, B. et al., 2021).

2 Results

Subsea permafrost distribution and state on the Arctic continental shelf was simulated from 400 kyr BP to the pre-industrial (1850 CE) using three model configurations: (1) the CLIMBER2 ice history (Ganopolski et al., 2010) and GMSL from Grant et al. (2014) without GIA (hereafter *legacy* run); (2) the ICE6G ice history (Peltier et al., 2015) and GMSL curve prior to the LGM from (Waelbroeck et al., 2002) without GIA (hereafter *base* run); and (3) the ICE6G ice history and GMSL curve prior to LGM from Waelbroeck et al. (2002) with GIA (hereafter *GIA* run, see Methods). The subsea permafrost calculation was extended from 1850 CE to 3000 CE for the *GIA* and *base* runs using 17 different future ice sheet configurations based on the ISMIP6 ensemble (Chambers et al., 2021; Greve & Chambers, 2021) and climate forcing scenarios from the IPCC-AR6 (see Methods). The *GIA* run is presented hereafter, and we demonstrate and explain how changes in model setup between the *legacy* run, which resembles P. P. Overduin et al. (2019) (see

Methods), the *base* run, and the *GIA* run affect our modeling results. Permafrost was modeled between 187 m below and 18 m above present-day sea level at every location on the Arctic continental shelf and nearshore. The total modeled permafrost area is defined as the sum of modeled regions whose depth profiles included terrestrial or subsea permafrost. Sedimentation rates, mineral conductivity, geothermal heat flux, and vertical conductive heat flux were parameterized following P. P. Overduin et al. (2019). At every time step in the resulting permafrost distribution, we removed permafrost from locations where warm bottom water from present-day rivers, deltas, and estuaries likely precludes permafrost formation (P. P. Overduin et al., 2019).

2.1 Past evolution and present-day extent

The temporal evolution of subsea permafrost, as measured by mean thickness, responds to Earth's sawtooth history of ice volume change (Fig. 1). The mean thickness of permafrost in the total model area increases during glaciations as sea level falls and exposes the shelf to cold air temperatures. Subsea permafrost is generally absent during these times since the continental shelves are exposed. Deglaciation inundates continental shelves and turns terrestrial permafrost into subsea permafrost, which quickly thaws as warm ocean waters increase temperatures on the shelf. After interglacials, subsea permafrost continues to thaw until it disappears or is converted to terrestrial permafrost by falling sea level. In the *GIA* run, the mean thickness of permafrost in our total modeled area peaks at 500-550 m during glacial maxima and thins to 125-150 m by the end of interglacials (Fig. 1B).

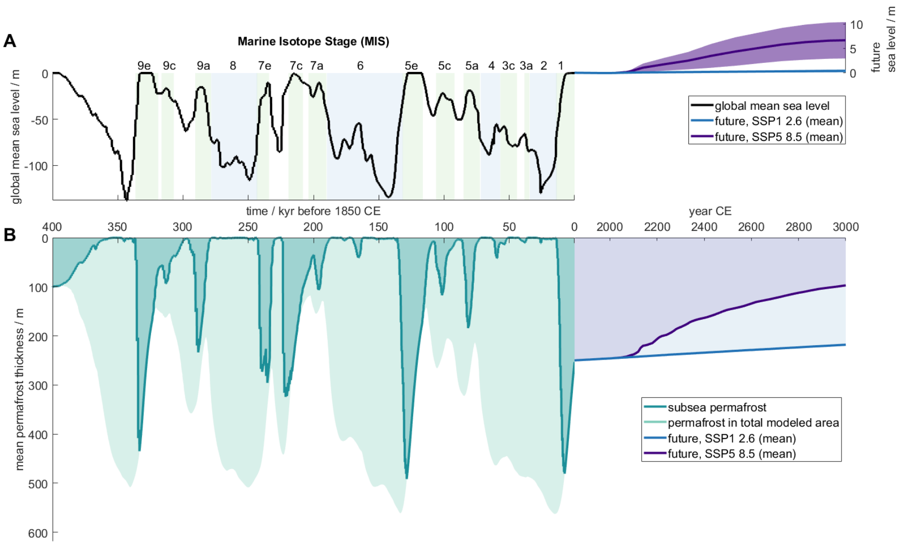

Figure 1. Timeseries of subsea permafrost thickness and global mean sea level (GMSL). (A) GMSL from Waelbroeck et al. (2002) and Peltier et al. (2015) (past); Chambers et al. (2021) and Greve, Calov, et al. (2020) (future, see Methods). Marine isotope stages (MIS) are indicated following Railsback et al. (2015). (B) Mean subsea permafrost thickness (dark teal) between 400 kyr BP and 1850 CE for the *GIA* run. Mean permafrost thickness in the total modeled area (light teal). Subsea permafrost thickness for low (SSP1-2.6, blue) and high (SSP5-8.5, purple) emissions scenarios.

Based on the *GIA* run, subsea permafrost presently underlies 1.8×10^6 km^2 of the Arctic continental shelf and has a mean thickness of 253 m. Subsea permafrost reaches a maximum thickness of 708 m in shallow sediments offshore of Yukagir in the central Laptev Sea. Permafrost that exceeds a thickness of 500 m also underlies the shallow central Kara Sea and the westernmost coastline of the Alaskan North Slope, while much of the deeper Chukchi and East Siberian Seas cover subsea permafrost that is less than 200 m thick (Fig. 2A, see Fig. 5A for locations).

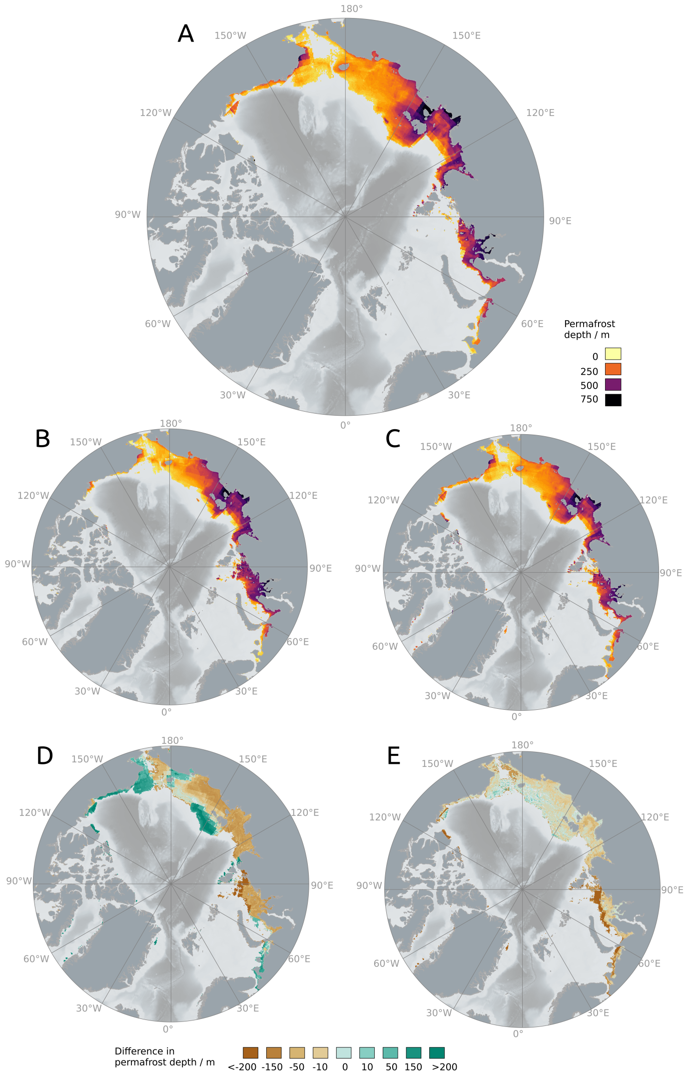

Figure 2. (A) Subsea permafrost thickness at 1850 for the *GIA* model run. (B) Same as (A), but for the *legacy* model run. (C) Same as (A) but with the *base* run. (D) The difference in permafrost thickness between the *base* and *legacy* model runs (i.e. C-B). (E) The difference in permafrost thickness between the *GIA* and *base* model runs (i.e. A-C). Areas in (D) and (E) with >200 m difference in permafrost thickness are locations where additional permafrost is introduced in the *base* and *GIA* cases, respectively.

2.1.1 *Ice history & Global mean sea-level curve*

The choice of ice history affects present-day subsea permafrost. When compared to subsea permafrost estimates from the *legacy* run, adopting the *base* run results in thicker present-day cryotic sediment on the deep Russian continental shelf and nearly all the Canadian arctic by >50 m, but yields thinner cryotic sediment on much of the shallow Russian continental shelf by 200-250 m and in the eastern Kara Sea by >500 m (fig. 2B).

These patterns are explained by the differing GMSL and ice distributions in the *base* and *legacy* runs. GMSL in the *base* run is generally higher early in glacial intervals (MIS 11b-10b, 9d-8b, 7b-6b, 5d-3a) than GMSL in the *legacy* run, but lower during peak glacials (MIS 10a, 7d, 6a, 2, Fig. 3). Higher early-glacial GMSL inhibits the formation of shallow subsea permafrost by decreasing subaerial exposure time; lower peak-glacial GMSL enhances subsea permafrost formation on the deep shelf (Fig. 3). The >500 m thickness difference in the eastern Kara Sea is caused by differences in ice distribution. CLIMBER2, which drives the *legacy* run and employs the SICOPOLIS polythermal ice model, simulates a small Eurasian Ice Sheet (EIS) with little ice east of the western Kara Sea at glacial maxima, while in the *base* run maximal ice extent crosses the Kara Sea to the Severnaya Zemlya archipelago, inhibiting permafrost formation in that region. While the GMSL and ice history of the last glacial cycle have the largest impact on present-day subsea permafrost distribution, conditions during the earlier glacial cycles, particularly the penultimate cycle, also affect present-day permafrost thickness and ice content. Overall, using the *base* ice history decreases the area of seafloor presently underlain by permafrost by $4{\times}10^5$ km^2 and the mean thickness of that permafrost by 44 m compared to the *legacy* run.

Though sea level modulates the fraction of time that Arctic sediments spend exposed to air, water, and ice, the variable that drives permafrost formation directly is surface forcing temperature. Mean surface forcing temperature was calculated at each location from the local history of sea-level, glacial load, and air temperature (Fig. 4, see Methods). Since air temperatures are chosen to be the same in the *legacy*, *base*, and *GIA* runs, changes in surface forcing temperature are driven by varying sea-level curves and ice sheet histories, and therefore resemble permafrost thickness changes in Fig. 2B & C. The change from *legacy* to *base* run diminishes temperature forcing—i.e. the mean surface temperatures of the *base* run are cooler than those relative to the *legacy* run—in much of the Canadian arctic, the deepest areas of the Laptev and East Siberian Seas, around the New Siberian Islands, and near the White Sea (Fig. 4A). In these regions, subsea permafrost in the *base* run is thicker than in the *legacy* run 2B). Areas where *base* run mean temperature forcing is warmer than the *legacy* run, and subsea permafrost consequently thinner, include the Laptev Sea and the shallower parts of the East Siberian and Chukchi Seas.

2.1.2 *GIA effects on present-day subsea permafrost distribution*

Present-day subsea permafrost distribution and state is significantly influenced by GIA. The inclusion of GIA in the model reduces the area of Arctic shelf that is underlain by cryotic sediments at 1850 CE from $2.1{\times}10^6$ to $1.8{\times}10^6$ km^2, i.e. by 14 %.

GIA causes systematic deviations in RSL on the Arctic continental shelf. These deviations are chiefly due to glacial loading, peripheral bulge dynamics, and hydro-isostasy. Gravitational effects tend to be smaller since the rebounding Earth in part counteracts the gravitational effects from melting ice sheets (Supplemental Fig. S1). The EIS inhibits permafrost formation in all but the shallowest areas of the Barents and Kara Seas. In those shallow regions where permafrost is present, direct isostatic loading increases sea level when covered by the EIS, as seen in the >80 m rise in GIA in the Kara Sea during glacial maxima (Fig. 5C, D). Peripheral bulges around the EIS and Laurentide ice

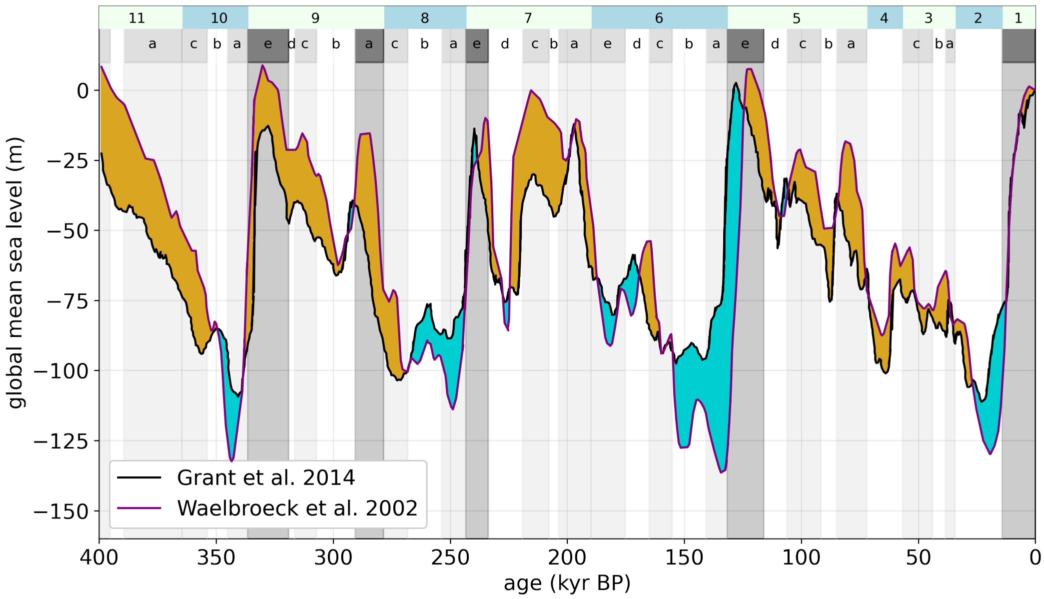

Figure 3. Global mean sea-level curves between 400 ka and present. Blue filled envelope represents times when the GMSL curve of Waelbroeck et al. (2002), used in the *GIA* and *base* runs, is deeper than the GMSL curve of Grant et al. (2014), used in the *legacy* run; brown envelope represents times when the Waelbroeck et al. (2002) curve is shallower. Numbers and letters along top edge represent Marine Isotope Stages (MIS) as defined in Railsback et al. (2015). Darker grey bars indicate MIS substages during which substantial subsea permafrost is formed.

.

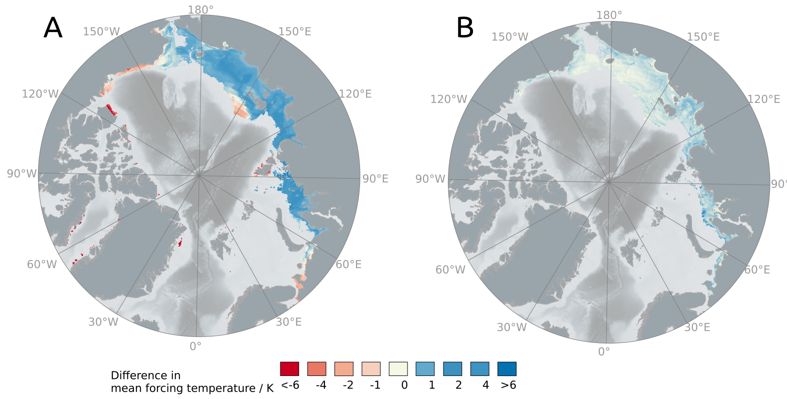

Figure 4. Mean temperature forcing change between subsea permafrost experiments. (A) Difference in mean forcing temperature between *legacy* and *base* runs. (B) Difference in mean forcing temperature between *base* and *GIA* runs.

lead to negative GIA (RSL is lower than GMSL) (Fig. 5B) and the shape and location of this feature evolves through time.

Outboard of the peripheral bulge, hydro-isostasy exerts a dominant influence on RSL (Fig. 5B). Hydro-isostasy is the GIA response to changing water load: ice melt dur-

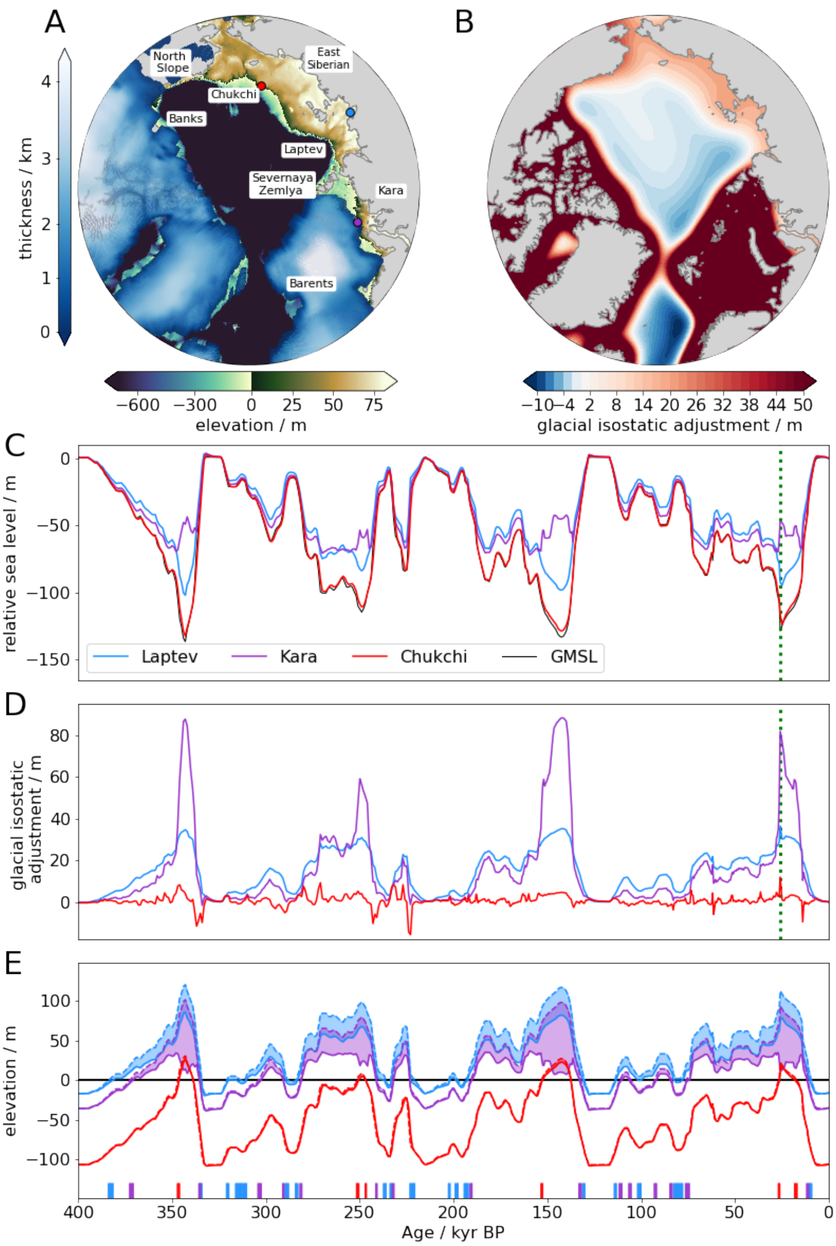

Figure 5. (A) Topography of the Arctic continental shelf at Last Glacial Maximum (26 ka) in meters above sea level. Colored dots indicate exemplary locations in the East Siberian (red), Laptev (blue), and Kara (purple) seas. Other labeled sites include Banks Island, the Alaskan North Slope, the Chukchi Sea, the Severnaya Zemlya archipelago, and the Barents Sea. (B) Difference between RSL and GMSL at Last Glacial Maximum (26 ka). (C) Timeseries of global mean sea level (GMSL, black) as well as relative sea level (RSL) at exemplary sites. Dashed green line indicates Last Glacial Maximum. (D) Difference between RSL and GMSL for exemplary sites. (E) Elevation of exemplary sites. Solid lines indicate elevation including GIA; dashed lines indicate elevation without GIA; the difference is highlighted in solid fill. Vertical dashes indicate times when each site is inundated in the GIA run but not the base run.

ing interglacials adds water to the ocean, which depresses the oceanic crust and elevates continental margins; ice sheet growth during glacials unloads oceans and causes continental margin subsidence (Chappell, 1974). The hydro-isostatic effect is strongest in the Laptev, East Siberian, Chukchi Seas as well as on the Alaskan North Slope. During glaciations, water unloading leads to rebound of the oceans and subsidence of continents. Since the water masses rise with the rebounding ocean floor, sea level at the shelf break follows the global mean while sea level at the modern coastline is higher than the global mean (Fig. 5C). This process is reversed during transgressions.

On average, the *GIA* run leads to higher sea level / lower elevations on the continental shelf, which causes mean temperatures on the shelf to be warmer in the *GIA* run compared to the *base* run (Fig. 4B). This causes generally thinner subsea permafrost at the present in the *GIA* run compared to the *base* run (Fig. 2E). Inboard of the Laurentide and Eurasian peripheral bulges, the main GIA effect that influences permafrost is direct isostatic loading, which increasess inundation (Fig. 5B). For example, along the western edge of Banks Island and in the Barents and Kara Seas, including GIA causes a thinning of present-day subsea permafrost that ranges from >200 m thinner on the deeper shelf to ∼50 m thinner in the shallowest sediments (Fig. 2A). Beyond the peripheral bulge, hydro-isostasy causes cryotic sediment in areas of shallow bathymetry, such as the Laptev Sea, to thin by up to 50 m, while permafrost underlying deeper areas—e.g. distal parts of the East Siberian, Chuchki, and Beaufort Seas—thickens by up to 10 m.

In addition to this broad-stroke GIA signal, temperature and hence permafrost extent is also dependent on the amount of time that the land is exposed. Land exposure time is a function of topography: GIA exposes shallow locations more frequently throughout glacial cycles, but deep locations only at the beginnings of glacial maxima (Fig. 5E). This leads to the more granular detail in the difference in permafrost thickness between the *GIA* run and the *base* run (Fig. 2E). In total, inclusion of GIA decreases the area of continental shelf underlain by subsea permafrost by 3×10^5 km^2 and the mean thickness of that permafrost by 11 m.

2.2 Future permafrost evolution

The future evolution of subsea permafrost depends on the amount of anthropogenic emissions in the next century. Under a low emissions scenario (SSP1-2.6), subsea permafrost as modeled in the *GIA* run will continue its historical rate of thinning to thin on average by ∼30 m to a mean of ∼211 m by 3000 CE. This thinning will be concentrated in the central Laptev and Kara Seas due to the thicker present-day permafrost stocks in those areas. With low 21st century emissions, virtually no areas of seafloor presently underlain by permafrost will completely lose it in the next thousand years (Fig. 6). Under the high emissions scenario (SSP5-8.5), on the other hand, subsea permafrost will thin more than ∼38 m everywhere by 2300 CE. This thinning will result in the disappearance of permafrost—with disappearance defined as permafrost thinning to <50 m—at the outer edge of the Russian arctic continental shelf and southern Alaska. By 3000 CE, subsea permafrost will have thinned an average of ∼153 m, a >60 % loss relative to 1850 CE, which will result in subsea permafrost disappearing from the Chukchi Sea, nearly all the Canadian arctic, much of the East Siberian Sea, and deep areas of the Laptev and Kara Seas.

There is strong correlation between the pre-industrial thickness of subsea permafrost and its time of disappearance (Fig. 7). Under low emissions, no permafrost thicker than 100 m at 1850 CE thaws before 3000 CE. Under high emissions, all permafrost thinner than 100 m at 1850 CE, but none thicker than 200 m, disappears before 2300 CE. And by 3000 CE, under high emissions only permafrost more than 160 m thick at 1850 CE remains.

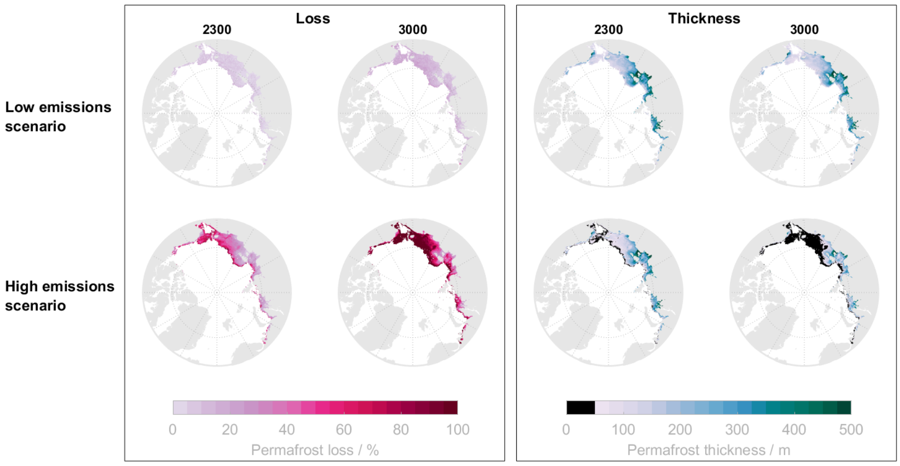

Figure 6. Modeled subsea permafrost loss percentage and thickness by 2300 and 3000 CE for low (SSP1-2.6) and high (SSP5-8.5) emissions scenarios.

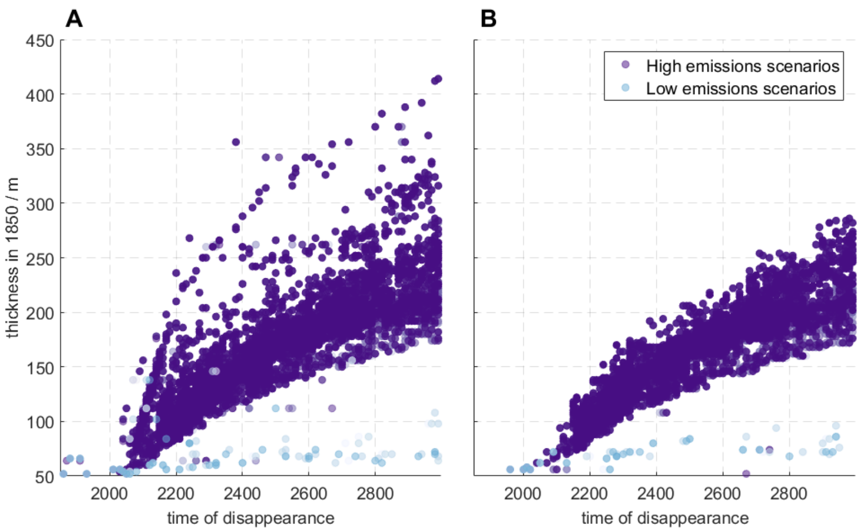

Figure 7. Time when the permafrost at each location is thinner than 50 m for (A) *base* and (B) *GIA* run.

2.2.1 GIA effects on future subsea permafrost distribution

GIA affects future subsea permafrost in two ways: (1) 400,000 years of GIA influence leads to thinner present-day subsea permafrost in shallow-water regions (see Fig. 2), thereby reducing the thickness of the permafrost remaining and (2) GIA affects future sea-level change and causes local sea level to differ from the mean. The former is the significantly more important factor and has been described above. We will expand here on the latter.

Future GIA acts to decrease RSL everywhere on the Arctic shelf, which has a small negative effect on the amount of future subsea permafrost. Less RSL rise decreases the area of newly flooded land, which leads to mean subsea permafrost thickness in the high emissions scenario thinning by $\sim$3 m more by 3000 in the *GIA* run than in the *base* run. The GIA effect is modest relative to GMSL rise, however, which increases 8.6 m$\pm$4.6 m by 3000 CE in the high emissions scenarios. During previous interglacials, rising sea level temporarily increased mean subsea permafrost thickness by increasing the area of inundation. However, when ocean bottom temperatures exceed 0 °C—projected to occur around ∼2100 CE with high future emissions (Wilkenskjeld et al., 2021)—any newly-flooded permafrost will rapidly thaw from above as well as below. Beyond this ocean temperature tipping point, future sea-level rise produces no gain in subsea permafrost.

The total effect of GIA causes earlier subsea permafrost disappearance. For instance, all permafrost thinner than 100 m at 1850 disappears ∼25 years faster in the *GIA* run compared to the *base* run (2260 vs. 2290 CE, Fig. 7). And unlike in the *base* run, in the *GIA* run no permafrost thicker than 200 m at 1850 CE disappears prior to 2400 CE (Fig. 7A).

3 Discussion

The large influence that different ice sheet histories have on our modeled present-day subsea permafrost distributions highlights the role that late Quaternary ice sheets play in permafrost formation. Ice sheets control permafrost directly beneath them because ice thickness and subglacial hydrology modulate sub-ice temperatures. It has also long been known that terrestrial permafrost can influence ice sheet evolution (e.g. Licciardi et al., 1998; Clark et al., 1999; Tarasov & Peltier, 2007). We demonstrate that ice sheets also influence subsea permafrost hundreds to thousands of kilometers distant due to the gravitational and deformational effects of GIA. This finding supports a growing body of evidence that climatic teleconnections have shaped permafrost evolution in the 20^{th} century (e.g. Romanovsky et al., 2010) and the geologic past (e.g. Li et al., 2021), and will likely continue to do so in the future (Ehlers et al., 2022).

Deep uncertainty, defined as uncertainty stemming from disagreement or ignorance about the processes that drive a system, hampers precise projections of sea level over the next century (Kopp et al., 2017, 2019). Projecting over the next millennium further expands the pool of uncertainty sources. Large uncertainties also surround ice sheet histories for the past four glacial cycles.

While full quantification of these uncertainties is beyond the scope of this study, first steps towards harnessing subsea permafrost as an ice sheet constraint are already possible using our results. Using the ICE-6G ice history results in thinner permafrost in the Eastern Laptev sea, a finding that better aligns with evidence from seismic surveys suggesting that ice-bonded permafrost exists only in Eastern Laptev sediments inboard of the 60 m isobath (Bogoyavlensky et al., 2023). Use of the ICE-6G ice history also increases the modeled thickness and lower boundary of present-day ice-saturated subsea permafrost on the Beaufort shelf (Fig. 2D). This finding better aligns with seismic and borehole data that find the lowermost ice-saturated permafrost in the Beaufort Sea at an average depth of 500 m (Canadian) and 460 m (Alaskan), and mean thickness of Alaskan Beaufort Sea ice-saturated sediments of 200 m (Fig. 8, Ruppel & Kessler, 2017; Hu et al., 2013). Improved data-model fit indicates that the combination of ICE6G and the Waelbroeck et al. (2002) GMSL curve may represent the Beaufort Sea's history of ice cover, inundation, and subaerial exposure better than CLIMBER2 and the GMSL curve from Grant et al. (2014) do.

However, modeled Beaufort Sea permafrost in the *GIA* run is still significantly thinner and shallower than observations, suggesting that subsea permafrost in this region may be influenced by processes not accounted for in our model. These processes include permafrost formation beneath shallow ice sheet margins, spatial variations in benthic temperatures driven by inflow of warm Atlantic water into the Arctic, changes in river and drainage basins, and spatiotemporally discrete sedimentation and erosion events such as glaciogenic debris flows, the transgression of which would produce additional syngenetic

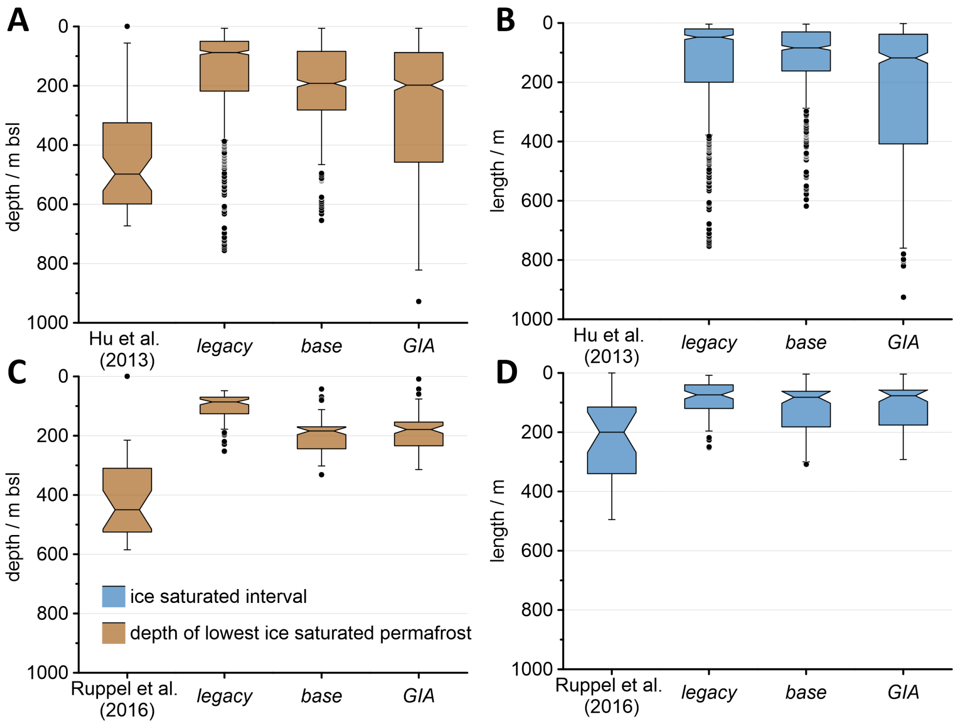

Figure 8. Comparison of borehole observations to modeled values for the depth of the lowermost ice saturated cell (A, C) and the length of the depth interval of ice-saturated sediment (B, D). Borehole data from the Canadian (A, B Hu et al., 2013) and Alaskan (C, D ?, ?) Beaufort shelf regions are compared to modeled values from the three runs (*legacy*, *base* and *GIA*) for all modeled locations bounded by the borehole coordinates. Note that the depth interval of ice-saturated sediment is not calculable from Hu et al. (2013)

.

subsea permafrost. Though inclusion of these factors exceeds this study's scope, they likely have significant impacts on subsea permafrost formation and should be included in future pan-Arctic permafrost models.

Beyond the Beaufort and Eastern Laptev Seas, the lack of observational constraints leaves the updates in subsea permafrost distribution made here open to future observational ground-truthing. Such is the case off the west coast of Banks Island, Canada, where our *GIA* run predicts no subsea permafrost but P. P. Overduin et al. (2019) map subsea permafrost that in places exceeds 200 m. Should future observational campaigns target regions such as Banks Island or the eastern Kara Sea, they will have the added benefit of constraining not only subsea permafrost itself but also the local glaciation histories of the Eurasian and Laurentide ice sheets.

Future work should focus investigation of the sensitivity of present-day permafrost to ice sheet variations during times when ice histories are especially uncertain. Those times include the LGM, where ice sheet modeling continues to disagree with sea level estimates of global ice volume (Simms et al., 2019); MIS-3 (57 kyr to 34 kyr BP, Railsback et al., 2015)), when recent evidence suggests GMSL may have been more than 20 m higher than modeled here (Waelbroeck et al., 2002; Pico et al., 2018; Dalton et al., 2022; Farmer et al., 2023); and the penultimate deglaciation, when the size of the EIS and its collapse history remain largely uncertain (Dendy et al., 2017). Future work could also test subsea permafrost's sensitivity to the history of the Siberian ice sheet, which during the penultimate and earlier glacial cycles may have held significant mass (?, ?). Differences in ice sheet loading during these intervals, and the accompanying sea-level variations, would produce characteristic spatial signatures in present-day permafrost. This line of inquiry points to subsea permafrost as an as-yet-untapped constraint on past ice sheet histories.

The analysis of subsea permafrost presented here has implications for the amount of organic carbon that subsea permafrost presently holds and therefore its potential as a future emitter of greenhouse gases. Recent structured expert assessment of subsea permafrost places present-day stocks of organic carbon and methane, respectively, at ~560 (170–740, 90 % confidence interval) and 45 (10–110) gigatons of carbon, and projects that subsea permafrost could emit 190 (45–590) Gt CO_2-equivalent (Sayedi et al., 2020). Our work suggests that present-day subsea permafrost is thinner than previously thought in shallow regions and in the western Russian arctic, in some areas by several hundred meters. We also find that the area of seafloor presently underlain by subsea permafrost is >25 % smaller than previously estimated. These findings reduce both the amount of organic carbon that subsea permafrost may hold and the amount of greenhouse gases that it may, through future thaw, release, though lack of consensus remains about what proportion of the CO_2 and methane released by subsea permafrost reaches the atmosphere (Mestdagh et al., 2017; Portnov et al., 2014). Projecting into the future, our results constrain the spatial distribution of future permafrost loss as well as the pace of its thaw. These findings can inform present planning for future community-based and industrial undertakings on the Arctic continental shelf, as such activities rely on accurate assessment of subsurface sediment characteristics.

Comparison of future climate projections with paleoclimatic analogues can give perspective on the effect that human activity has had on the climate system. We provide this context by comparing our projected rates of future subsea permafrost thinning to thinning rates over the past four glacial cycles (Fig. 9). Mean rates of past subsea permafrost thinning during interstadials have ranged from 5 m/kyr during MIS-9c to 31.2 m/kyr during MIS-7e (Fig. 9). In previous interglacial periods during which average subsea permafrost thickness exceeded 200 m, e.g. MIS 9e, 9a, 7e, 5e, 1, subsea permafrost thinned at an average rate of ~27 m/kyr. We project that subsea permafrost will thaw at a rate similar to 1850 speeds until 2050 (29 m/kyr) regardless of emissions scenario. After 2050, human activity in the 21st century will have a significant effect on subsea permafrost thinning rates. Under low emissions scenarios, the present rate of thinning continues to 3000 CE. High 21st century emissions, however, will accelerate thinning between 2050 and 2350 CE to > 8 times faster than the fastest thinning rate since MIS-9. Between 2350 and 3000 CE, thinning rates remain at 110 m/kyr, which is roughly four times faster than pre-industrial values.

Subsea permafrost thaw accelerates under the high emissions scenarios because the Arctic passes a climate tipping point. Loss of Arctic sea ice, included in our model via the modeled bottom water temperatures from Wilkenskjeld et al. (2021), spurs the Arctic to warm at a rate faster than the global mean (Dai et al., 2019). The positive feedback loop inherent in Arctic amplification – wherein lost sea ice lowers Arctic albedo, which hastens sea ice loss – leads to cascading effects on the Arctic climate system. These effects include the warming of Arctic shelf waters above zero degrees (Wilkenskjeld et al., 2021), a tipping point past which subsea permafrost thaw accelerates as it melts from both above and below. Though this acceleration is avoided under the low emissions scenario, under the high emissions scenario the tipping point occurs at ~2050 CE.

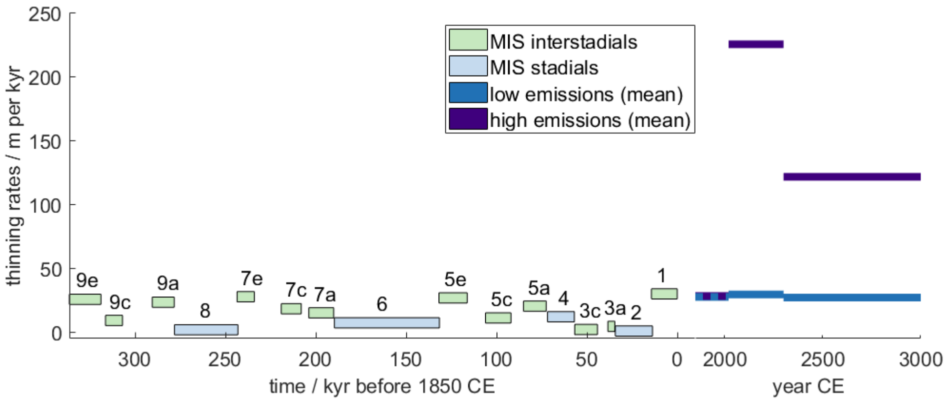

Figure 9. Mean thickness change rates between 400 kyr BP and 3000 CE. Horizontal lines denote mean rates of subsea permafrost thinning for each Marine Isotope Stage (MIS) during which subsea permafrost existed and for future predictions.

4 Conclusion

Our new pan-Arctic simulation of subsea permafrost from 400 kyr BP to 3000 CE enables an updated assessment of the history, present-day characteristics, and future evolution of subsea permafrost that accounts for the effects of GIA. We find that GIA influences subsea permafrost evolution everywhere on the continental shelf, with the deformational effects of ice sheet loading dominant in the Barents, Kara, and Beaufort Seas, and hydro-isostasy dominant in the Laptev, East Siberian, and Chukchi Seas. Our new subsea permafrost map based on the *GIA* run has 14 % less seafloor area underlain by permafrost and is 4.2 % thinner than the same run without GIA. Both runs update the ice cover and sea level forcing of the legacy run (cf. P. P. Overduin et al., 2019) resulting in even less permafrost (by 14 % area and 8 % thickness). The recent IPCC-AR6 report suggests that future permafrost thaw would be insufficient to trigger self-reinforcing acceleration in climate warming (Chen et al., 2021). The same is not true of the future effects of climate warming on subsea permafrost. Under a high emissions scenario that includes the loss of year-round Arctic sea ice, which is included in our modeling, self-reinforcing feedbacks in the climate system trigger rapid, irreversible acceleration of subsea permafrost thaw that begins in the next 30 years and persists so long as ocean bottom temperatures exceed 0 °C. This possible future adds yet more urgency to efforts to slow human emission of greenhouse gases in the next quarter century.

5 Methods

5.1 Permafrost model

Permafrost extent and composition were calculated from the output of a 1-D heat transfer model. We used CryoGrid 2, a 1-D heat diffusion model introduced by Westermann et al. (2013), which is a model that continues to develop. The current version is described in a release paper (Westermann et al., 2022) and the code is available at

https://github.com/CryoGrid/CryoGridCommunity_source/releases/tag/GMD

(accessed 20.05.2022). The model was implemented similarly to the implementation in P. P. Overduin et al. (2019), save that we changed the synthesized forcing temperature by using different sources for sea level, ice sheet histories, and began the model at 400 ka rather than 450 ka. We performed calculations at grid cell centers of the 12.5 km

EASE Grid 2.0 (Brodzik et al., 2012) and included any locations with modern elevations between 187 m below and 18 m above sea level (bsl, asl, Jakobsson et al., 2020).

Boundary conditions

The lower boundary condition for permafrost was temporally invariant heat flux drawn from the globally distributed data of Davies (2013). The upper boundary condition was temperature, either land surface, seabed or subglacial, as described in the following.

Historical land surface temperature was forced with air temperature from the CLIMBER2 intermediate complexity Earth System Model (Ganopolski et al., 2010). Under conditions of future sea-level change, some modeled locations may submerge or emerge, and thus require forcing with future land surface temperatures until submergence or following emergence. This applied to only a few locations in our modelling domain, usually next to the coast. In these few cases, constant temperatures equivalent to those during pre-industrial time (1850 CE) were applied. Though permafrost was removed from present-day locations where warm bottom water in deltaic and estuarine settings likely precludes permafrost formation, no assumptions were made about the locations of paleo rivers and estuaries. This likely results in a minor overestimation of subsea permafrost in those regions.

Historical seabed temperatures were forced as a function of water depth, based on observational data from the Siberian shelf area (Dmitrenko et al., 2011). Reductions in ice cover extent and duration are expected to warm the seabed since brine produced by freezing sea ice cools the seabed. Wilkenskjeld et al. (2021) shows warming of the seabed by up to 10 °C under more severe climate change scenarios such as Shared Socioeconomic Pathway 8.5 (SSP5-8.5) (Supplemental Fig. S2). The increase in seabed temperatures is strongly related to disappearance of sea ice. Our future seabed temperature forcing was adjusted by the spatial-mean anomaly of projected decadal mean seabed temperatures for either a low (SSP1-2.6) or high (SSP5-8.5) emissions scenario (Wilkenskjeld et al., 2021) from 1850 to 2950 CE, consistent for each run with the corresponding ice sheet model forcing (Tab. S1). Temperatures from 2950 to 3000 CE were held constant at 2950 CE level. Subglacial temperatures were treated as warm-based for ice masses exceeding 100 m in thickness and set to 0 °C, as in P. P. Overduin et al. (2019).

5.2 Glacial Isostatic Adjustment model

GIA was calculated following the algorithm of Kendall et al. (2005), which computes gravitationally self-consistent sea-level variations that are caused by ice and liquid water loading on a viscoelastic earth. Calculations include the effects of shoreline migration and the impact of load-induced Earth rotation changes on sea level (Mitrovica et al., 2005; Milne & Mitrovica, 1998). We assume a radially symmetric viscoelastic Earth structure with a viscosity following the VM5 profile (Peltier et al., 2015) and the elastic structure and density from the PREM seismic model (Dziewonski & Anderson, 1981).

Ice history 400 ka to 2015 CE

Our ice history from the Last Glacial Maximum (LGM) to 1950 CE follows ICE-6G (Peltier et al., 2015). The ICE-6G history was then extended back over four glacial cycles following the GMSL curve from Waelbroeck et al. (2002), which is based on RSL observations and δ^{18}O records from benthic foraminifera (Fig. 3). Ice sheet geometries prior to the LGM were chosen by finding the post-LGM ICE-6G geometry that best matches each pre-LGM GMSL value. For GMSL values prior to LGM that fall outside of the range of LGM to present values, we assume the closest available GMSL value. This assumption resulted in a present-day GMSL during MIS-9e and 5e since no template of ice collapse is available in the ICE-6G deglacial history. Though these times have higher than modern GMSL (e.g. de Gelder et al., 2022), this approximation is expected to have a negligible effect on the results presented here. There is evidence that the ice sheet configuration during the penultimate glacial maximum differed significantly from that during the last glacial maximum (Batchelor et al., 2019). We therefore followed the approach of Dendy et al. (2017) replacing the EIS geometries between 200 and 130 ka with reconstructions from (Lambeck, 1995; Lambeck et al., 2006) and pairing them with Laurentide ice sheet geometries chosen from the post-LGM ICE-6G history in order to maintain the GMSL curve of (Waelbroeck et al., 2002).

For the ice geometry between 1950 and 2015, we used the ice thickness from the Ice Sheet Model Intercomparison Project (ISMIP6, S. M. J. Nowicki et al., 2016; S. Nowicki et al., 2020). ICE-6G's 1950 CE ice extent is not in full agreement with the 1950 CE ice thicknesses from the Ice Sheet Model Intercomparison Project (ISMIP6, S. M. J. Nowicki et al., 2016; S. Nowicki et al., 2020). We therefore constructed a smooth transition from ICE6G to ISMIP6 ice extents by tapering the difference between the two models from 0 % to 100 % between 0 CE and 1950 CE, then added it to ICE6G. The GIA simulation was run from 400 kyr BP to 1950 CE with time steps of 100 yr, which were interpolated using nearest neighbour interpolation to the 100 yr timesteps of the permafrost simulation.

Ice history 2015 to 3000 CE

Between 2015 and 3000 we used an ensemble of 17 Antarctic and 14 Greenland ice models from the SICOPOLIS polythermal ice-sheet model (Greve, Calov, et al., 2020; Greve, Chambers, & Calov, 2020), which, following the ISMIP6 protocol, were produced with dynamic oceanic and atmospheric forcing between 2015 and the end of 2100 and constant forcing through 3000. See Chambers et al. (2021) and Greve and Chambers (2021) for full details on Antarctic and Greenland, respectively. AIS and GIS ensemble members with identical Generalized Circulation Model (GCM) forcing, ocean forcing, and emissions scenario (SSP/RCP) were paired. AIS members with no identical GIS analogues were paired with a GIS member produced by the same emissions scenario. See Table S1 for details the list of GIS/AIS pairings. The GIA simulation was run with time steps between 10 yr and 100 yr, which were interpolated using nearest neighbour interpolation to the 10 yr timesteps of the permafrost simulation.

5.3 Permafrost Model Output and Data Analysis

Model output included sediment temperature and composition at 2 m spacing over depth to 2 km below the land surface or seabed, at the modeled EASE Grid 2.0 locations. The temporal resolution of the output is 100 yr for the historic period until 1850 CE and 10 yr for the future projections.

The model was run over all possible permafrost locations, i.e. all locations on the EASE Grid 2.0 with current elevation between -187 and 18 masl as this encompasses the maximum range of RSL change in the forcing data. We also applied a filter to rule out locations in big river deltas and estuaries, including grid cells near the Ob and Lena rivers, St. Petersburg Gulf, the Baltic Sea, near Iceland, south of Kamchatka, and in the Bering Strait. Results were then further filtered, to include only locations that a) have been subaerial for at least 100 yr during the model period, b) are currently submerged and c) have modern permafrost deeper than what a theoretical modern steady state solution yields (cf. P. P. Overduin et al., 2019).

To evaluate possible future thinning rates of subsea permafrost, we calculated the mean projected thinning rates within the low (SPP1-2.6) and high (SSP5-8.5) emissions scenarios for the historic period (1850 - 2020 CE), the near future (2020 - 2300 CE) and the distant future (2300 - 3000 CE). For comparison, we calculated the mean thinning rate between minimum and maximum mean permafrost thickness for each MIS.

We compare our modeled lower permafrost bound to observations determined using a combination of well-log and temperature records from the Beaufort shelf (Canadian: Hu et al. (2013); Alaskan: Ruppel and Kessler (2017)). Most well-log records vary as a function of ice saturation of the sediment pore space (e.g. bulk sediment propagation velocity or electrical resistivty), whereas our modeled values reflect the depth of the 0°C isotherm. Values from Ruppel and Kessler (2017) are based on their assessment of intermediate ice saturation; only permafrost lower limit observations with a a data quaity of a or b were included from Hu et al. (2013). All modeled grid cells within the longitudinal range covered by the industry wells, are included, i.e. from the coastline out to the outer edge of permafrost occurrence. The proximity of the industry wells to the shoreline skews to thicker permafrost.

Observed lower bounds of permafrost are deeper than our models produce, and differences between the model runs are smaller (<55 m) than between mean modeled and mean observed (298 m, Ruppel and 274 m, Hu).

6 Acknowledgements

This work was supported by National Science Foundation grant OCE-18-41888 (RC, J). The project has received funding under the European Union's Horizon 2020 Research and Innovation Programme under grant agreement no. 773421 (FM, PPO).

References

Angelopoulos, M., Overduin, P. P., Miesner, F., Grigoriev, M. N., & Vasiliev, A. A. (2020). Recent advances in the study of Arctic submarine permafrost. *Permafrost and Periglacial Processes*, *31*(3), 442–453. doi: 10.1002/ppp.2061

Batchelor, C. L., Margold, M., Krapp, M., Murton, D. K., Dalton, A. S., Gibbard, P. L., … Manica, A. (2019, August). The configuration of Northern Hemisphere ice sheets through the Quaternary. *Nature Communications*, *10*(1), 3713. doi: 10.1038/s41467-019-11601-2

Bogoyavlensky, V., Kishankov, A., & Kazanin, A. (2023, February). Evidence of large-scale absence of frozen ground and gas hydrates in the northern part of the East Siberian Arctic shelf (Laptev and East Siberian seas). *Marine and Petroleum Geology*, *148*, 106050. doi: 10.1016/j.marpetgeo.2022.106050

Brodzik, M. J., Billingsley, B., Haran, T., Raup, B., & Savoie, M. H. (2012, June). EASE-Grid 2.0: Incremental but Significant Improvements for Earth-Gridded Data Sets. *ISPRS International Journal of Geo-Information*, *1*(1), 32–45. doi: 10.3390/ijgi1010032

Brothers, L. L., Herman, B. M., Hart, P. E., & Ruppel, C. D. (2016). Subsea ice-bearing permafrost on the U.S. Beaufort Margin: 1. Minimum seaward extent defined from multichannel seismic reflection data. *Geochemistry, Geophysics, Geosystems*, *17*(11), 4354–4365. doi: 10.1002/2016GC006584

Brown, J., Jr, O. J. F., Heginbottom, J. A., & Melnikov, E. S. (1997). Circum-Arctic map of permafrost and ground-ice conditions. *Circum-Pacific Map*(45). doi: 10.3133/cp45

Chambers, C., Greve, R., Obase, T., Saito, F., & Abe-Ouchi, A. (2021, December). Mass loss of the Antarctic ice sheet until the year 3000 under a sustained late-21st-century climate. *Journal of Glaciology*, 1–13. doi: 10.1017/jog.2021.124

Chappell, J. (1974, December). Late Quaternary glacio- and Hydro-Isostasy, on a Layered Earth. *Quaternary Research*, *4*(4), 405–428. doi: 10.1016/0033-5894(74)90037-4

Chen, D., Rojas, M., Samset, B., Cobb, K., Diongue, N., Edwards, P., … Tréguier, A.-M. (2021). Chapter 1: Framing, Context and Methods. In *Climate Change 2021: The Physical Science Basis. Contribution of Working Group I to the Sixth Assessment Report of the Intergovernmental Panel on Climate Change* (pp. 147–286). Cambridge, United Kingdom and New York, NY, USA: Cambridge University Press.

Clark, P. U., Alley, R. B., & Pollard, D. (1999, November). Northern Hemisphere Ice-Sheet Influences on Global Climate Change. *Science*, *286*(5442), 1104–1111. doi: 10.1126/science.286.5442.1104

Dai, A., Luo, D., Song, M., & Liu, J. (2019, January). Arctic amplification is caused by sea-ice loss under increasing CO2. *Nature Communications*, *10*(1), 121. doi: 10.1038/s41467-018-07954-9

Dalton, A. S., Pico, T., Gowan, E. J., Clague, J. J., Forman, S. L., McMartin, I., … Helmens, K. F. (2022, May). The marine δ18O record overestimates continental ice volume during Marine Isotope Stage 3. *Global and Planetary Change*, *212*, 103814. doi: 10.1016/j.gloplacha.2022.103814

Davies, J. H. (2013). Global map of solid Earth surface heat flow. *Geochemistry, Geophysics, Geosystems*, *14*(10), 4608–4622. doi: 10.1002/ggge.20271

de Gelder, G., Husson, L., Pastier, A.-M., Fernández-Blanco, D., Pico, T., Chauveau, D., … Pedoja, K. (2022, October). High interstadial sea levels over the past 420ka from the Huon Peninsula, Papua New Guinea. *Communications Earth & Environment*, *3*(1), 1–12. doi: 10.1038/s43247-022-00583-7

Dendy, S., Austermann, J., Creveling, J. R., & Mitrovica, J. X. (2017, September). Sensitivity of Last Interglacial sea-level high stands to ice sheet configuration during Marine Isotope Stage 6. *Quaternary Science Reviews*, *171*, 234–244. doi: 10.1016/j.quascirev.2017.06.013

Dmitrenko, I. A., Kirillov, S. A., Tremblay, L. B., Kassens, H., Anisimov, O. A., Lavrov, S. A., … Grigoriev, M. N. (2011). Recent changes in shelf hydrography in the Siberian Arctic: Potential for subsea permafrost instability. *Journal of Geophysical Research: Oceans*, *116*(C10). doi: 10.1029/2011JC007218

Dziewonski, A. M., & Anderson, D. L. (1981, June). Preliminary reference Earth model. *Physics of the Earth and Planetary Interiors*, *25*(4), 297–356. doi: 10.1016/0031-9201(81)90046-7

Ehlers, T. A., Chen, D., Appel, E., Bolch, T., Chen, F., Diekmann, B., … Zhu, L. (2022, November). Past, present, and future geo-biosphere interactions on the Tibetan Plateau and implications for permafrost. *Earth-Science Reviews*, *234*, 104197. doi: 10.1016/j.earscirev.2022.104197

Farmer, J. R., Pico, T., Underwood, O. M., Cleveland Stout, R., Granger, J., Cronin, T. M., … Sigman, D. M. (2023, January). The Bering Strait was flooded 10,000 years before the Last Glacial Maximum. *Proceedings of the National Academy of Sciences*, *120*(1), e2206742119. doi: 10.1073/pnas.2206742119

Farrell, W. E., & Clark, J. A. (1976, September). On Postglacial Sea Level. *Geophysical Journal of the Royal Astronomical Society*, *46*(3), 647–667. doi: 10.1111/j.1365-246X.1976.tb01252.x

Fox-Kemper, B., Hewitt, H.T., Xiao, C., Aðalgeirsdóttir, G., Drijfhout, S.S., Edwards, T.L., … Yu, Y. (2021). 2021: Ocean, cryosphere and sea level change. *The Sixth Assessment Report of the Intergovernmental Panel on Climate Change.*.

Friedlingstein, P., Jones, M. W., O'Sullivan, M., Andrew, R. M., Bakker, D. C. E., Hauck, J., … Zeng, J. (2022, April). Global Carbon Budget 2021. *Earth System Science Data*, *14*(4), 1917–2005. doi: 10.5194/essd-14-1917-2022

Friedlingstein, P., O'Sullivan, M., Jones, M. W., Andrew, R. M., Hauck, J., Olsen, A., … Zaehle, S. (2020, December). Global Carbon Budget 2020. *Earth System Science Data*, *12*(4), 3269–3340. doi: 10.5194/essd-12-3269-2020

Ganopolski, A., Calov, R., & Claussen, M. (2010, April). Simulation of the last glacial cycle with a coupled climate ice-sheet model of intermediate complexity. *Climate of the Past*, *6*(2), 229–244. doi: 10.5194/cp-6-229-2010

Gilfillan, D., Marland, G., Boden, T., & Andres, R. (2019, March). *Global, Regional, and National Fossil-Fuel CO2 Emissions* [Text]. https://energy.appstate.edu/CDIAC.

Grant, K. M., Rohling, E. J., Ramsey, C. B., Cheng, H., Edwards, R. L., Florindo, F., … Williams, F. (2014, September). Sea-level variability over five glacial cycles. *Nature Communications*, *5*(1), 5076. doi: 10.1038/ncomms6076

Greve, R., Calov, R., Obase, T., Saito, F., Tsutaki, S., & Abe-Ouchi, A. (2020, September). *ISMIP6 future projections for the Antarctic ice sheet with the model SICOPOLIS* (Tech. Rep.). Zenodo. doi: 10.5281/zenodo.4035932

Greve, R., & Chambers, C. (2021). *Mass loss of the Greenland ice sheet until the year 3000 under a sustained late-21st-century climate.* doi: 10.31223/X5TK7C

Greve, R., Chambers, C., & Calov, R. (2020, August). *ISMIP6 future projections for the Greenland ice sheet with the model SICOPOLIS* (Tech. Rep.). Zenodo. doi: 10.5281/zenodo.3971252

Hu, K., Issler, D., Chen, Z., & Brent, T. (2013). *Permafrost investigation by well logs, and seismic velocity and repeated shallow temperature surveys, Beaufort-Mackenzie Basin.* doi: 10.4095/293120

Jakobsson, M., Mayer, L. A., Bringensparr, C., Castro, C. F., Mohammad, R., Johnson, P., … Zinglersen, K. B. (2020, July). The International Bathymetric Chart of the Arctic Ocean Version 4.0. *Scientific Data*, *7*(1), 176. doi: 10.1038/s41597-020-0520-9

Jones, B. M., Arp, C. D., Jorgenson, M. T., Hinkel, K. M., Schmutz, J. A., & Flint, P. L. (2009). Increase in the rate and uniformity of coastline erosion in Arctic Alaska. *Geophysical Research Letters*, *36*(3). doi: 10.1029/2008GL036205

Kendall, R. A., Mitrovica, J. X., & Milne, G. A. (2005, June). On post-glacial sea level - II. Numerical formulation and comparative results on spherically symmetric models. *Geophysical Journal International*, *161*(3), 679–706. doi: 10.1111/j.1365-246X.2005.02553.x

Klemann, V., Heim, B., Bauch, H. A., Wetterich, S., & Opel, T. (2015, November). Sea-level evolution of the Laptev Sea and the East Siberian Sea since the last glacial maximum. *arktos*, *1*(1), 1. doi: 10.1007/s41063-015-0004-x

Kopp, R. E., DeConto, R. M., Bader, D. A., Hay, C. C., Horton, R. M., Kulp, S., … Strauss, B. H. (2017). Evolving Understanding of Antarctic Ice-Sheet Physics and Ambiguity in Probabilistic Sea-Level Projections. *Earth's Future*, *5*(12), 1217–1233. doi: 10.1002/2017EF000663

Kopp, R. E., Gilmore, E. A., Little, C. M., Lorenzo-Trueba, J., Ramenzoni, V. C., & Sweet, W. V. (2019). Usable Science for Managing the Risks of Sea-Level Rise. *Earth's Future*, *7*(12), 1235–1269. doi: 10.1029/2018EF001145

Lakeman, T. R., & England, J. H. (2014, September). Late Wisconsinan glaciation and postglacial relative sea-level change on western Banks Island, Canadian Arctic Archipelago. *Quaternary Research*, *80*(1), 99–112. doi: 10.1016/j.yqres.2013.02.001

Lambeck, K. (1995, January). Constraints on the Late Weichselian ice sheet over the Barents Sea from observations of raised shorelines. *Quaternary Science Reviews*, *14*(1), 1–16. doi: 10.1016/0277-3791(94)00107-M

Lambeck, K., Purcell, A., Funder, S., KJæR, K. H., Larsen, E., & Moller, P. (2006). Constraints on the Late Saalian to early Middle Weichselian ice sheet of Eurasia from field data and rebound modelling. *Boreas*, *35*(3), 539–575. doi: 10.1080/03009480600781875

Li, T.-Y., Baker, J. L., Wang, T., Zhang, J., Wu, Y., Li, H.-C., … Edwards, R. L. (2021, September). Early Holocene permafrost retreat in West Siberia amplified by reorganization of westerly wind systems. *Communications Earth & Environment*, *2*(1), 1–11. doi: 10.1038/s43247-021-00238-z

Licciardi, J. M., Clark, P. U., Jenson, J. W., & Macayeal, D. R. (1998, January). Deglaciation of a Soft-Bedded Laurentide Ice Sheet. *Quaternary Science Reviews*, *17*(4), 427–448. doi: 10.1016/S0277-3791(97)00044-9

Mestdagh, T., Poort, J., & De Batist, M. (2017, June). The sensitivity of gas hydrate reservoirs to climate change: Perspectives from a new combined model for permafrost-related and marine settings. *Earth-Science Reviews*, *169*, 104–131. doi: 10.1016/j.earscirev.2017.04.013

Milne, G. A., & Mitrovica, J. X. (1998, April). Postglacial sea-level change on a rotating Earth. *Geophysical Journal International*, *133*(1), 1–19. doi: 10.1046/j.1365-246X.1998.1331455.x

Mitrovica, J. X., Wahr, J., Matsuyama, I., & Paulson, A. (2005, May). The rotational stability of an ice-age earth. *Geophysical Journal International*, *161*(2), 491–506. doi: 10.1111/j.1365-246X.2005.02609.x

Nicolsky, D., & Shakhova, N. (2010, January). Modeling sub-sea permafrost in the East Siberian Arctic Shelf: The Dmitry Laptev Strait. *Environmental Research Letters*, *5*(1), 015006. doi: 10.1088/1748-9326/5/1/015006

Nicolsky, D. J., Romanovsky, V. E., Romanovskii, N. N., Kholodov, A. L., Shakhova, N. E., & Semiletov, I. P. (2012). Modeling sub-sea permafrost in the East Siberian Arctic Shelf: The Laptev Sea region. *Journal of Geophysical Research: Earth Surface*, *117*(F3). doi: 10.1029/2012JF002358

Nowicki, S., Goelzer, H., Seroussi, H., Payne, A. J., Lipscomb, W. H., Abe-Ouchi, A., … van de Wal, R. (2020, July). Experimental protocol for sea level projections from ISMIP6 stand-alone ice sheet models. *The Cryosphere*, *14*(7), 2331–2368. doi: 10.5194/tc-14-2331-2020

Nowicki, S. M. J., Payne, A., Larour, E., Seroussi, H., Goelzer, H., Lipscomb, W., … Shepherd, A. (2016, December). Ice Sheet Model Intercomparison Project (ISMIP6) contribution to CMIP6. *Geoscientific Model Development*, *9*(12), 4521–4545. doi: 10.5194/gmd-9-4521-2016

Overduin, P., Wetterich, S., Günther, F., Grigoriev, M. N., Grosse, G., Schirrmeister, L., … Makarov, A. S. (2016). Coastal dynamics and submarine permafrost in shallow water of the central Laptev Sea, East Siberia. *Cryosphere*, *10*, 1449–1462. doi: 10.5194/tc-10-1449-2016

Overduin, P. P., von Deimling, T. S., Miesner, F., Grigoriev, M. N., Ruppel, C., Vasiliev, A., … Westermann, S. (2019). Submarine Permafrost Map in the Arctic Modeled Using 1-D Transient Heat Flux (SuPerMAP). *Journal of Geophysical Research: Oceans*, *124*(6), 3490–3507. doi: 10.1029/2018JC014675

Peltier, W. R., Argus, D. F., & Drummond, R. (2015, January). Space geodesy constrains ice age terminal deglaciation: The global ICE-6G_C (VM5a) model. *Journal of Geophysical Research: Solid Earth*, *120*(1), 450–487. doi: 10.1002/2014JB011176

Pico, T., Birch, L., Weisenberg, J., & Mitrovica, J. X. (2018, September). Refining the Laurentide Ice Sheet at Marine Isotope Stage 3: A data-based approach combining glacial isostatic simulations with a dynamic ice model. *Quaternary Science Reviews*, *195*, 171–179. doi: 10.1016/j.quascirev.2018.07.023

Portnov, A., Mienert, J., & Serov, P. (2014). Modeling the evolution of climate-sensitive Arctic subsea permafrost in regions of extensive gas expulsion at the West Yamal shelf. *Journal of Geophysical Research: Biogeosciences*, *119*(11), 2082–2094. doi: 10.1002/2014JG002685

Proshutinsky, A., Ashik, I. M., Dvorkin, E. N., Häkkinen, S., Krishfield, R. A., & Peltier, W. R. (2004). Secular sea level change in the Russian sector of the Arctic Ocean. *Journal of Geophysical Research: Oceans*, *109*(C3). doi: 10.1029/2003JC002007

Proshutinsky, A., Pavlov, V., & Bourke, R. H. (2001). Sea level rise in the Arctic Ocean. *Geophysical Research Letters*, *28*(11), 2237–2240. doi: 10.1029/2000GL012760

Railsback, B., Gibbbard, P., Head, M., Voarintsoa, R., & Toucanne, S. (2015, March). An optimized scheme of lettered marine isotope substages for the last 1.0 million years, and the climatostratigraphic nature of isotope stages and substages. *Quaternary Science Reviews*, *111*, 94–106. doi: 10.1016/j.quascirev.2015.01.012

Romanovskii, N. N., Hubberten, H. W., Gavrilov, A. V., Tumskoy, V. E., & Kholodov, A. L. (2004, June). Permafrost of the east Siberian Arctic shelf and coastal lowlands. *Quaternary Science Reviews*, *23*(11), 1359–1369. doi: 10.1016/j.quascirev.2003.12.014

Romanovsky, V. E., Drozdov, D. S., Oberman, N. G., Malkova, G. V., Kholodov, A. L., Marchenko, S. S., ... Vasiliev, A. A. (2010). Thermal state of permafrost in Russia. *Permafrost and Periglacial Processes*, *21*(2), 136–155. doi: 10.1002/ppp.683

Ruppel, C. D., & Kessler, J. D. (2017). The interaction of climate change and methane hydrates. *Reviews of Geophysics*, *55*(1), 126–168. doi: 10.1002/2016RG000534

Sayedi, S. S., Abbott, B. W., Thornton, B. F., Frederick, J. M., Vonk, J. E., Overduin, P., ... Frei, R. J. (2020, December). Subsea permafrost carbon stocks and climate change sensitivity estimated by expert assessment. *Environmental Research Letters*, *15*(12), 124075. doi: 10.1088/1748-9326/abcc29

Schirrmeister, L., Kunitsky, V., Grosse, G., Wetterich, S., Meyer, H., Schwamborn, G., ... Siegert, C. (2011, August). Sedimentary characteristics and origin of the Late Pleistocene Ice Complex on north-east Siberian Arctic coastal lowlands and islands – A review. *Quaternary International*, *241*(1), 3–25. doi: 10.1016/j.quaint.2010.04.004

Shakhova, N., Semiletov, I., Leifer, I., Sergienko, V., Salyuk, A., Kosmach, D., ... Gustafsson, Ö. (2014, January). Ebullition and storm-induced methane release from the East Siberian Arctic Shelf. *Nature Geoscience*, *7*(1), 64–70. doi: 10.1038/ngeo2007

Simms, A. R., Lisiecki, L., Gebbie, G., Whitehouse, P. L., & Clark, J. F. (2019, February). Balancing the last glacial maximum (LGM) sea-level budget. *Quaternary Science Reviews*, *205*, 143–153. doi: 10.1016/j.quascirev.2018.12.018

Tarasov, L., & Peltier, W. R. (2007). Coevolution of continental ice cover and permafrost extent over the last glacial-interglacial cycle in North America. *Journal of Geophysical Research: Earth Surface*, *112*(F2). doi: 10.1029/2006JF000661

Waelbroeck, C., Labeyrie, L., Michel, E., Duplessy, J. C., McManus, J. F., Lambeck, K., ... Labracherie, M. (2002, January). Sea-level and deep water temperature changes derived from benthic foraminifera isotopic records. *Quaternary Science Reviews*, *21*(1), 295–305. doi: 10.1016/S0277-3791(01)00101-9

Westermann, S., Ingeman-Nielsen, T., Scheer, J., Aalstad, K., Aga, J., Chaudhary, N., ... Langer, M. (2022, June). *The CryoGrid community model (version 1.0) – a multi-physics toolbox for climate-driven simulations in the terrestrial cryosphere* (Preprint). Cryosphere. doi: 10.5194/gmd-2022-127

Westermann, S., Schuler, T. V., Gisnås, K., & Etzelmüller, B. (2013, April). Transient thermal modeling of permafrost conditions in Southern Norway. *The Cryosphere*, *7*(2), 719–739. doi: 10.5194/tc-7-719-2013

Wilkenskjeld, S., Miesner, F., Overduin, P. P., Puglini, M., & Brovkin, V. (2021, September). Strong Increase of Thawing of Subsea Permafrost in the 22nd Century Caused by Anthropogenic Climate Change. *The Cryosphere Discussions*, 1–18. doi: 10.5194/tc-2021-231